

DNS of high temperature effects on compressible isotropic turbulence

Gokul Ramanathan* and Shankar Ghosh†

Indian Institute of Technology Madras, Chennai, Tamil Nadu, 600036, India

High temperature effects on homogeneous decaying isotropic turbulence are studied using Direct Numerical Simulations (DNS). A Fourier-spectral compressible flow solver is developed for the purpose. To account for the high temperature effects, a local thermodynamic equilibrium based physical model for air is suggested. At high temperatures, both thermodynamic and transport properties of air are found to be significantly different from those predicted using a calorically perfect gas model. The effects of these properties on evolution of turbulent statistics are studied and comparisons are made with a calorically perfect gas model. Budgets are computed for turbulent kinetic energy and enstrophy to explain the results obtained using the high temperature model.

I. Introduction

Compressible isotropic turbulence has been studied in detail in the past. Theoretical work includes that of Kovaszny (1953) who performed a perturbation analysis of the compressible, viscous and heat conducting Navier-Stokes equations and identified vorticity, entropy and acoustic modes to characterise the turbulence. Chu and Kovaszny (1958) developed a consistent higher order perturbation theory to characterise the non-linearity in the Navier-Stokes equations in terms of the interactions between the modes. Samtaney et. al. (2001) conducted DNS studies of decaying compressible isotropic turbulence at moderate fluctuation Mach numbers and Taylor Reynolds numbers and found that the presence or absence of fluctuations in thermodynamic quantities have a negligible effect on the decay of turbulent kinetic energy. Ristorcelli and Blaisdell (1997) developed an asymptotic theory for statistical closure of compressible isotropic turbulence. Otto Zeman (1990) developed second order models for unforced isotropic turbulence in the compressible regime, including modelling dilatational dissipation and pressure-dilatation correlation. Erlebacher et. al. (1990) divided the turbulent velocity field into solenoidal and irrotational parts and performed DNS of incompressible and compressible isotropic turbulence using this velocity decomposition. Blaisdell (1991) performed DNS studies of compressible isotropic turbulence and found that the compressibility effects depend on the initial conditions.

As the temperature of air increases, certain physical processes like vibrational excitation, dissociation and ionisation of air molecules and resulting atoms start becoming important. As a result, the thermodynamic and transport properties of air at high temperatures differ significantly from those obtained using a calorically perfect assumption. In this work, effects of the thermodynamic and transport properties are studied by suggesting a high temperature model for air. Local thermodynamic equilibrium (L.T.E.) is assumed as the time scales associated with the equilibration of chemical reactions are typically much smaller than the time scales associated with the turbulence.

This paper is organised as follows. Section II contains a description of the different physical models for air used in the simulations. Section III describes the numerical method used and validation results for the same. Section IV shows simulation results and section V contains a brief summary of the work.

*Graduate Research student, Department of Aerospace Engineering.

†Assistant Professor, Department of Aerospace Engineering.

II. Physical Model

II.A. Governing equations

Governing equations are the non-dimensional 3D compressible Navier-Stokes equations:

$$\frac{\partial \rho}{\partial t} + \frac{\partial(\rho u_j)}{\partial x_j} = 0, \quad (1)$$

$$\frac{\partial(\rho u_i)}{\partial t} + \frac{\partial(\rho u_i u_j)}{\partial x_j} = -\frac{\partial}{\partial x_j} \left[p \delta_{ij} - \frac{\mu}{Re} \left(\frac{\partial u_i}{\partial x_j} + \frac{\partial u_j}{\partial x_i} - \frac{2}{3} \frac{\partial u_k}{\partial x_k} \delta_{ij} \right) \right], \quad (2)$$

$$\begin{aligned} \frac{\partial(\rho e_T)}{\partial t} + \frac{\partial(\rho e_T u_j)}{\partial x_j} &= \frac{\partial}{\partial x_j} \left[-p u_j + \frac{\mu}{Re} \left(\frac{\partial u_i}{\partial x_j} + \frac{\partial u_j}{\partial x_i} - \frac{2}{3} \frac{\partial u_k}{\partial x_k} \right) u_i \right] \\ &\quad + \frac{\partial}{\partial x_j} \left(K_t \frac{\partial T}{\partial x_j} \right). \end{aligned} \quad (3)$$

These equations are non-dimensionalized as follows:

$$\begin{aligned} x_i &= x_i^*/l_0^*, & u_i &= u_i^*/c_0^*, & t &= t^* c_0^*/l_0^* \\ \rho &= \rho^*/\rho_0^*, & p &= p^*/\rho_0^* c_0^{*2}, & T &= T^*/T_0^* \\ \mu &= \mu^*/\mu_0^*, & \kappa &= \kappa^*/\kappa_0^* \end{aligned} \quad (4)$$

In the above equations, ‘*’ superscript is used to denote dimensional variables. The dimensional background quantities are denoted by a ‘*’ superscript and a ‘0’ subscript. c_0^* is the speed of sound at the temperature T_0^* . Thus, all dimensional background quantities are based on this temperature. In this paper, T_0^* is taken to be 300K. K_t is the non-dimensional coefficient to the temperature gradient $\frac{\partial T}{\partial x_i}$ which takes on different forms based on the physical model used as discussed in section II.B.

The total energy per unit mass e_T is given by

$$e_T = e + \frac{1}{2} u_i u_i, \quad (5)$$

where e is the internal energy per unit mass. The non-dimensional parameter in the above set of equations is the computational Reynolds number Re given by

$$Re = \rho_0^* c_0^* l_0^* / \mu_0^*. \quad (6)$$

II.B. Physical Models

II.B.1. Model 1

For model 1, air is considered to be an calorically perfect ideal gas. Therefore the properties of air are calculated based on a constant specific heats model. The non-dimensional equation of state in this case is given by

$$P = \rho T / \gamma. \quad (7)$$

The internal energy e is given non-dimensionally by

$$e = \frac{T}{\gamma(\gamma - 1)}, \quad (8)$$

where γ for air is 1.4. The coefficient of viscosity is obtained from the non-dimensional power law

$$\mu = T^{0.67}. \quad (9)$$

The Prandtl number is given by

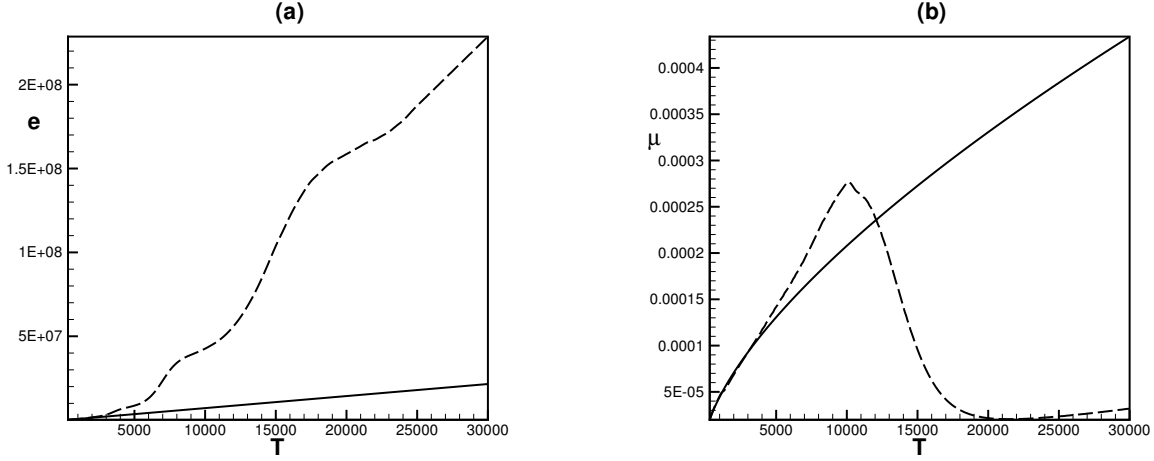


Figure 1. Variation of (a) internal energy and (b) specific gas constant with temperature for model 1 and model 2. — represents model 1 and - - - represents model 2.

$$Pr = \frac{\mu^* C_p^*}{k^*}. \quad (10)$$

For air, $Pr = 0.7$ is used. Also, K_t in this case is

$$K_t = \frac{\mu}{(\gamma - 1) Re Pr}. \quad (11)$$

II.B.2. Model 2

Model 2 takes into account high temperature effects resulting from dissociation and ionization of different species. The equation of state for model 2 is given by

$$P = \rho R(T) T, \quad (12)$$

where $R(T) = R^*(T)/(\gamma * R_0^*)$. The rest of the thermodynamic and transport variables are obtained using a 11 species air model consisting of N_2 , O_2 , NO , N , O , N_2^+ , O_2^+ , NO^+ , N^+ , O^+ and e^- . At L.T.E., each of these species are individually in equilibrium. Thus, the equilibrium composition can be obtained from the law of mass-action. Once the equilibrium composition is obtained the thermodynamic and transport properties of air can be determined by minimization of Gibbs free energy, along with the use of mass conservation and electrical neutrality equations (Boulos et. al. 1994).

The effect of radiation has been neglected in this model. K_t takes on the form

$$K_t = \frac{\kappa}{Re Pr_0 (\gamma - 1)}, \quad (13)$$

where Pr_0 is the Prandtl number based on the dimensional background values and has a value of 0.7. Figure 1 shows plots of internal energy e and the specific gas constant R as a function of temperature at atmospheric pressure for models 1 and 2. All quantities are dimensional. Model 1 assumes a linear relationship between internal energy and temperature. Model 2 agrees with model 1 till around 2000K. But at higher temperatures, the two models vary significantly. For instance, at around 12000 K, internal energy as predicted by model 2 is about five times that of model 1 as shown in figure 1a. So at higher temperatures, a calorifically perfect gas model is clearly insufficient to accurately represent the flow conditions. This statement is further supported by the variation of dynamic viscosity with temperature for both the models as shown in figure 1b. While model 1 predicts a power law form of increase of viscosity with temperature, Model 2 shows a sharp decrease in viscosity with increase in temperature beyond 10000K. It is important to note that even other models for viscosity like Sutherland's model (Sutherland 1893) do not predict this decrease in viscosity with increase in temperature.

III. Numerical Method

A Fourier-spectral based parallel compressible Navier-Stokes flow solver has been developed to study the problem. A uniform Cartesian grid can be defined as

$$\begin{aligned} x_i &= \frac{i-1}{N_x} L_x & i &= 1, \dots, N_x, \\ y_j &= \frac{j-1}{N_y} L_y & j &= 1, \dots, N_y, \\ z_k &= \frac{k-1}{N_z} L_z & k &= 1, \dots, N_z, \end{aligned} \quad (14)$$

where N_i and L_i denote the number of grid points and length of domain respectively along the i direction. A function $f(x, y, z)$ can be represented on this cartesian grid in terms of a discrete fourier transform

$$f_{i,j,k} = \sum_{k_x=-N_x/2}^{N_x/2-1} \sum_{k_y=-N_y/2}^{N_y/2-1} \sum_{k_z=-N_z/2}^{N_z/2-1} \hat{f}_{k_x,k_y,k_z} e^{i(\vec{k} \cdot \vec{x})}, \quad (15)$$

where \vec{k} is the vector of wavenumbers whose components are k_x , k_y and k_z and \vec{x} is the position vector in physical space. The Fourier coefficients \hat{f}_{k_x,k_y,k_z} are given by

$$\hat{f}_{k_x,k_y,k_z} = \sum_{i=1}^{N_x} \sum_{j=1}^{N_y} \sum_{k=1}^{N_z} f_{i,j,k} e^{-i(\vec{k} \cdot \vec{x})}. \quad (16)$$

Spatial derivatives are then obtained in the Fourier space as

$$\frac{\widehat{\partial f}}{\partial x_\alpha} = i k_\alpha \hat{f}, \quad \frac{\widehat{\partial^2 f}}{\partial x_\alpha \partial x_\alpha} = -k_\alpha^2 \hat{f}. \quad (17)$$

Inverse Fourier transforms give spatial derivatives in the physical space. A skew symmetric representation

$$\frac{\partial(fg)}{\partial x_i} = \frac{1}{2} \left[\frac{\partial(fg)}{\partial x_i} + f \frac{\partial g}{\partial x_i} + g \frac{\partial f}{\partial x_i} \right], \quad (18)$$

is used for the nonlinear terms to suppress aliasing errors. A fourth order Runge-Kutta explicit time integration method is implemented for time advancement.

III.A. Solver validation

The solver has been validated using the following problems.

III.A.1. Periodic shock tube problem

The domain of the periodic shock tube problem consists of a region of high pressure and density separated on both sides from regions of low pressure and density. The initial background temperature is 300K. Reynolds number and Prandtl number are 515 and 0.7 respectively. The boundary conditions are periodic. At $t=0$, the separation between the high and low pressure regions is removed and the pressure gradients force the fluid to start moving from the high pressure region to low pressure regions on either side. The gradients are strong enough to produce a pair of shocks propagating in opposite directions. The non-dimensional domain length is 2π which is resolved using 128 grid points. Figure 2a shows the profiles of density, pressure, temperature and stream-wise velocity. The computed numerical solution for the periodic shock tube problem at non dimensional time $t=1$ is compared with the simulation of Ghosh (2008) and a good agreement is obtained.

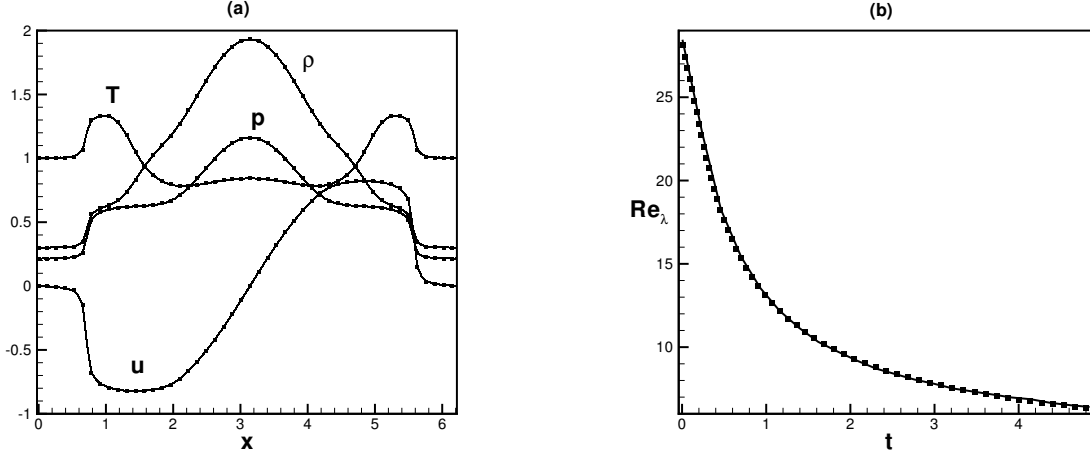


Figure 2. Validation results for (a) Periodic Shock Tube where — denotes the reference (Ghosh 2008) and ■ denotes our results and (b) Taylor Reynolds number for isotropic turbulence where — denotes the reference (Blaisdell 1991) and ■ denotes our results.

III.A.2. Decaying isotropic turbulence

Simulation of decaying isotropic turbulence is carried out in a domain of non dimensional size $2\pi \times 2\pi \times 2\pi$. This simulation uses a resolution of $96 \times 96 \times 96$ grid points in x, y and z directions. Periodic boundary conditions are imposed on all boundaries. Initial data required for the simulation are generated following Rogallo (1981). The initial energy spectrum used is a top-hat spectrum with energy between wave numbers 8 and 16. Initial turbulent Mach number M_t for the simulation is 0.3. The simulation results have been compared against those of Blaisdell (1991). Figure 2b shows the time evolution of Taylor Reynolds number Re_λ . The agreement is very good.

IV. Simulation Results

IV.A. Initial conditions for Isotropic turbulence

The initial conditions for compressible isotropic turbulence has been generated using the method suggested by Ristorcelli and Blaisdell (1997). The initial turbulent flow-field is assumed to be weakly compressible. It is shown that as a consequence of a nonzero turbulent mach number, there are finite thermodynamic and dilatational fluctuations associated with the initial turbulent flow-field. The procedure to generate this flow-field is briefly described below.

Firstly, a small Mach number expansion of the compressible Navier-Stokes equations about the initial background quantities is constructed with the assumption that $M_t \ll 1$. Thus the velocity field is decomposed according to

$$u_i = v_i + \epsilon^2 w_i + \dots, \quad (19)$$

where $\epsilon^2 = \gamma M_t^2$, v_i are the solenoidal velocity fluctuations obtained using a procedure described by Rogallo (1981) and w_i are the compressible velocity fluctuations. The thermodynamic variables are also similarly decomposed as the sum of a mean state and a perturbation about that mean state. When the expressions for the velocity and thermodynamic variables are substituted in the governing equations, neglecting viscous terms and retaining only lowest order terms, the following equations are obtained.

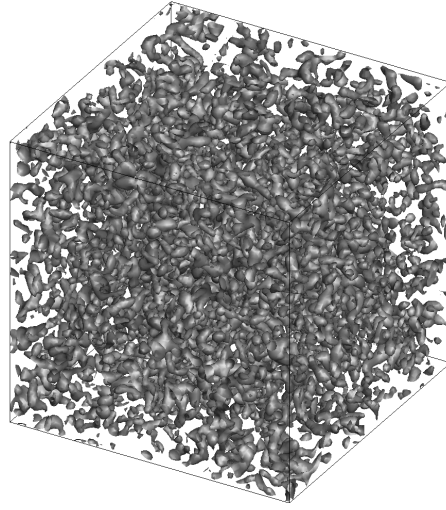


Figure 3. Isotropic turbulence initial flow field visualization using iso-contours of vorticity magnitude.

$$\frac{\partial v_i}{\partial x_i} = 0, \quad (20)$$

$$\frac{\partial^2 p_1}{\partial x_j \partial x_j} = -\frac{\partial^2 (v_i v_j)}{\partial x_i \partial x_j}, \quad (21)$$

$$\frac{\partial v_i}{\partial t} + v_p \frac{\partial v_i}{\partial x_p} + \frac{\partial p_1}{\partial x_i} = 0. \quad (22)$$

Equation 20 is a zeroth order measure of compressibility. In order to obtain a weakly compressible flow-field, a first order measure of compressibility is introduced as

$$\frac{\partial p_1}{\partial t} + v_k \frac{\partial p_1}{\partial x_k} = -\gamma d, \quad (23)$$

where d is the dilatation in the above equation which is the divergence of the compressible velocity fluctuations w_i . Equation 21 is a Poisson equation for the pressure fluctuations which is solved first. Then, the time derivative of the pressure fluctuations is solved for. It is obtained as:

$$\frac{\partial^2}{\partial x_j \partial x_j} \left(\frac{\partial p_1}{\partial t} \right) = 2 \frac{\partial^2}{\partial x_i \partial x_j} \left[\left(v_k \frac{\partial v_i}{\partial x_k} + \frac{\partial p_1}{\partial x_i} \right) v_j \right]. \quad (24)$$

The pressure fluctuations and their temporal derivatives are now used to solve for the dilatation given by equation 23. The compressible velocity fluctuations are then obtained in Fourier space using

$$\hat{w}_j = -(k_j/k^2) \hat{d}. \quad (25)$$

The temperature and density fluctuations can be obtained from the pressure fluctuations and the linearized isentropic relations

$$\rho_1 = (1/\gamma) p_1, \quad (26)$$

$$T_1 = [(\gamma - 1)/\gamma] p_1. \quad (27)$$

Figure 3 shows a three dimensional visualization of the initial flow field generated using the above procedure. Isotropic turbulence is visualized using iso-contours of vorticity magnitude.

Model	T	μ	ρ	p	K_t	R	Re	Re_λ
1	1	1	1	0.714	0.007	0.714	515	62.122
2	1	1	1	0.714	0.007	0.714	515	62.122

Table 1. Comparison of initial values of parameters for the simulations at 300K. All values have been non-dimensionalized with Model 1 values at 300K.

IV.B. Decaying isotropic turbulence simulation at 300 K for models 1 and 2

Simulations of decaying isotropic turbulence are carried out for models 1 and 2 at an initial mean temperature of 300K. Table 1 shows the initial non-dimensional values for the different simulations performed at 300 K. The initial parameters are chosen such that the same initial Re_λ is ensured at the same initial mean temperature T_0 for both models. The initial energy spectrum used for the incompressible velocity is a power four spectrum of the following form

$$E(k) = 16 \left(\frac{2}{\pi} \right)^{\frac{1}{2}} \left(\frac{u_0^2}{k_0} \right) \exp \left(-\frac{2k^2}{k_0^2} \right), \quad (28)$$

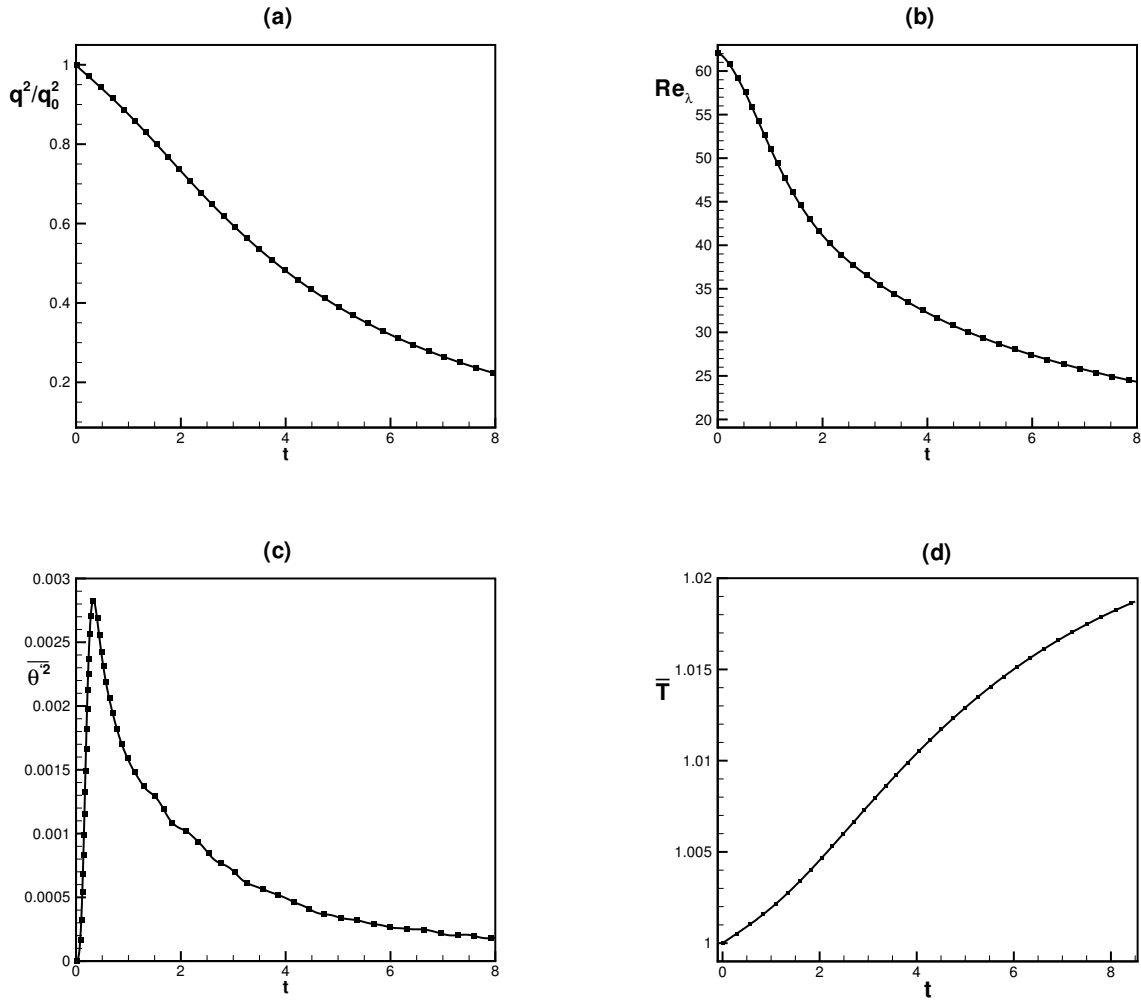


Figure 4. Comparison of turbulence statistics between model 1 and model 2 at 300 K: (a) normalized turbulent kinetic energy, (b) Taylor Reynolds number, (c) dilatation and (d) mean temperature. — denotes model 1 and ■ denotes model 2

where k_0 is the wavenumber corresponding to the peak in the energy spectrum and u_0 is root mean square velocity. The value of k_0 is 5. M_t for the simulation is 0.3. The non-dimensional domain size is $2\pi \times 2\pi \times 2\pi$. This simulation uses a resolution of $256 \times 256 \times 256$ grid points in x, y and z directions. Figure 4a shows the normalized turbulent kinetic energy evolution in time. Figure 4b shows the time evolution of Re_λ , with an initial value of 62.122. Figure 4c shows the mean square dilatation which rises initially and then decreases in time. Figure 4d represents the mean temperature which rises from the initial value of 300K. The good agreement between results obtained from models 1 and 2 is to be expected as at these temperatures model 2 should physically reduce to model 1.

IV.C. Decaying isotropic turbulence at 8000 K for models 1 and 2

The initial value of Re_λ for both models is taken to be 137.08 at a non-dimensional $T = 26.667$. Table 2 shows the initial non-dimensional values for parameters in simulations performed at 8000 K. Figure 6 shows the time evolution of various turbulent statistics. The rates of decay of turbulent kinetic energy (figure 6a) and Re_λ (figure 6b) for model 2 are higher than that of model 1. This can be explained based on the dissipation. For compressible isotropic turbulence, dissipation in non-dimensional form is given by Blaisdell (1991) as

$$\epsilon = \underbrace{\frac{\bar{\mu}}{Re} \overline{\omega'_i \omega'_i}}_{\text{solenoidal dissipation} - \epsilon_s} + \underbrace{\frac{4}{3} \frac{\bar{\mu}}{Re} \overline{\frac{\partial u'_i}{\partial x_i} \frac{\partial u'_j}{\partial x_j}}}_{\text{dilatational dissipation} - \epsilon_d}, \quad (29)$$

where the prime denotes fluctuating quantities and the overbar denotes volumetric averages. The dilatation (figure 6c) and vorticity (figure 9) as predicted by model 2 are significantly larger than model 1. Thus, total dissipation is larger for model 2, resulting in faster decay of q^2 and Re_λ shown in figures 6a and 6b respectively.

Figure 5 shows the relative contributions of the solenoidal and dilatational components to the total dissipation for both the models. The solenoidal component is shown to match the total dissipation very closely whereas the dilatational component is seen to be orders of magnitude smaller. For model 1, the dilatational dissipation is three orders of magnitude smaller (figure 5a) and for model 2, it is two orders of magnitude smaller (figure 5b). Although the relative importance of the dilatational component is higher for model 2 than for model 1, it is still small compared to the solenoidal component. Thus, it can be concluded that solenoidal dissipation is the main source of dissipation.

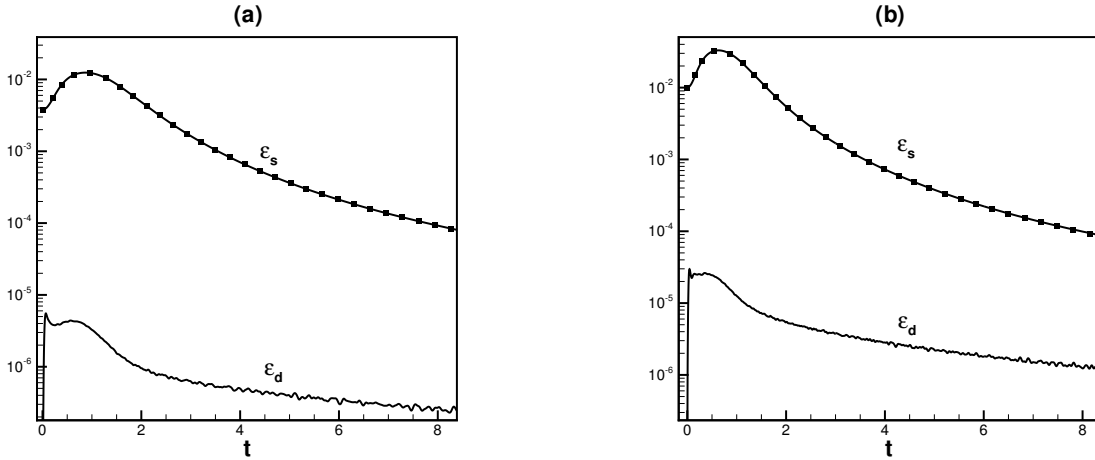


Figure 5. (a) Shows the components of dissipation for model 1 at 8000K and (b) shows the components of dissipation for model 2 at 8000K. — represents solenoidal dissipation, - - - represents dilatational dissipation and ■ denotes total dissipation.

Another observation is the time evolution of mean temperature as shown in figure 6d. It is interesting to note that the rate of increase of mean temperature is smaller for model 2 than model 1, resulting in

smaller mean temperatures after a significant part of the turbulent kinetic energy has decayed. This can be attributed to the presence of multiple modes of internal energy at high temperatures for model 2. The dissipated turbulent kinetic energy goes into various internal energy modes which at these temperatures include vibrational excitation. Also, part of the energy is used for chemical reactions. On the other hand, in model 1 the turbulent kinetic energy is dissipated only into the translational - rotational internal energy mode causing the temperature to rise more in comparison to model 2.

Model	T	μ	ρ	p	K_t	R	Re	Re_λ
1	26.667	9.024	1	19.048	1.611^{-02}	0.714	2000	137.08
2	26.667	11.324	1.933^{-02}	0.700	4.798^{-03}	1.358	90413	137.08

Table 2. Comparison of initial values of parameters for simulations at 8000K. All values have been non-dimensionalized with Model 1 values at 300K.

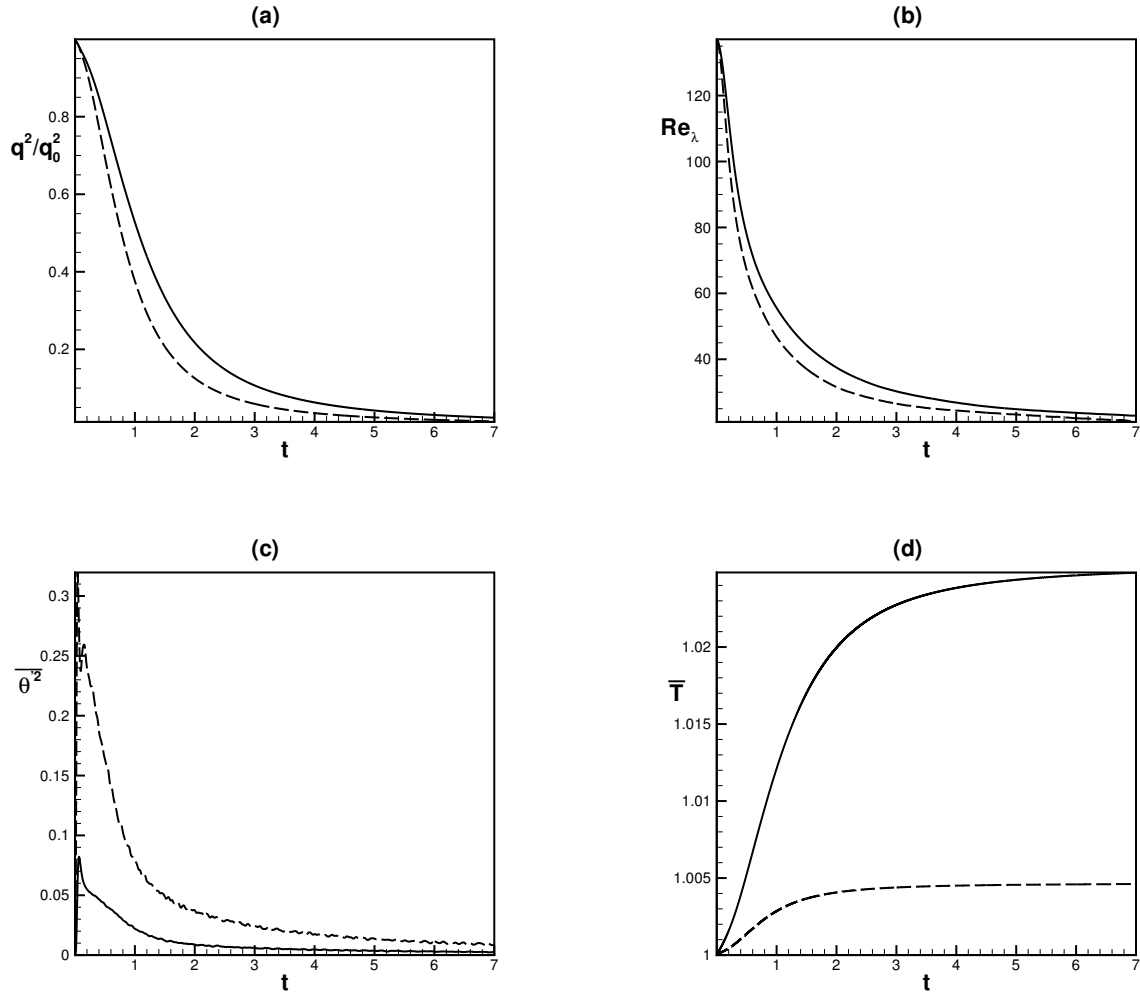


Figure 6. Comparison of turbulence statistics between model 1 and model 2 at 8000 K: (a) normalized turbulent kinetic energy, (b) Taylor Reynolds number, (c) dilatation and (d) mean temperature non-dimensionalized with initial background mean temperature of 8000K, — represents model 1 and - - - represents model 2

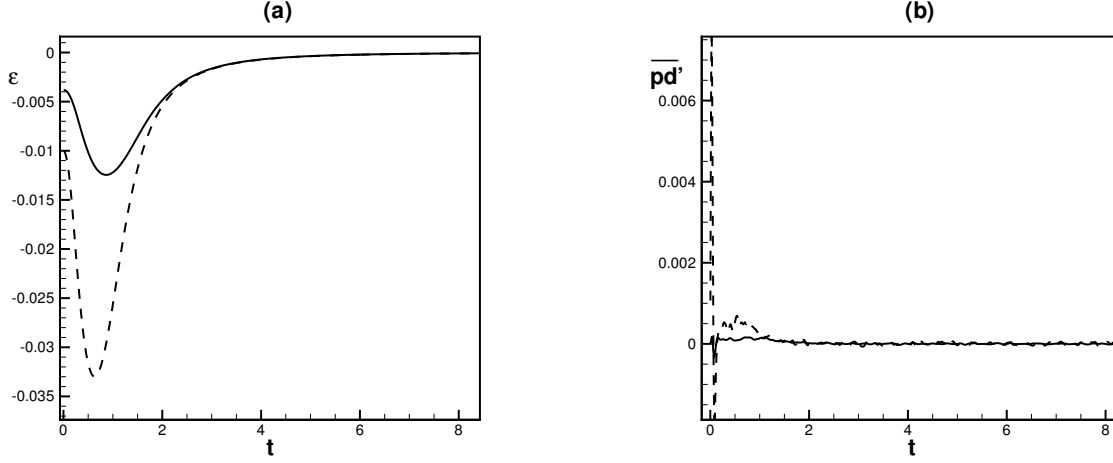


Figure 7. Shows the results of the turbulent kinetic energy budget for models 1 and 2 at 8000 K. (a) Shows the dissipation term and (b) Shows the pressure dilatation term. — represents model 1 and - - - represents model 2.

In order to better understand the distribution of turbulent kinetic energy, budgets for different terms on the right hand side of the turbulent kinetic energy equation

$$\begin{aligned} \frac{\partial}{\partial t} (\overline{\rho \tilde{k}}) = & \underbrace{-\nabla \cdot (\overline{\rho \tilde{k} \underline{u}})}_{\text{convection}} - \underbrace{(\overline{\rho \underline{u}'' \otimes \underline{u}''}) : \nabla \underline{\tilde{u}}}_{\text{production}} - \underbrace{\overline{\tau : \nabla \underline{u}''}}_{\text{dissipation}} + \underbrace{\nabla \cdot \left(\overline{\underline{u}'' \cdot \tau} - \rho \underline{u}'' \left(\frac{1}{2} \underline{u}'' \cdot \underline{u}'' \right) - \overline{p' \underline{u}''} \right)}_{\text{diffusion}} \\ & - \underbrace{\overline{\underline{u}'' \cdot \nabla (\overline{p})}}_{\text{pressure work}} + \underbrace{\overline{p' \nabla \cdot \underline{u}''}}_{\text{pressure dilatation}}, \end{aligned} \quad (30)$$

are computed. Here, k is given by $1/2(\underline{u}'' \cdot \underline{u}'')$ and the underlined quantities are vectors. Of the terms shown in equation 30, the only non-zero terms are the dissipation and the pressure dilatation terms. Figures 7a and 7b show the dissipation and pressure dilatation terms plotted in time for both the models respectively. As explained earlier, dissipation is stronger for model 2 in comparison to model 1. The pressure dilatation for model 2 is also noted to be initially stronger than model 1 as observed by the spike in figure 7b. Later, the pressure dilatation for both the models becomes negligible. Also, note that the dissipation term is significantly stronger than the pressure dilatation term.

Budgets are computed for terms on the right hand side of the enstrophy transport equation to understand the evolution of enstrophy over time. For compressible isotropic turbulence, the equation can be written as

$$\begin{aligned} \frac{\partial}{\partial t} (\overline{\omega'_i \omega'_i}) = & \overline{\omega'_i \omega'_j \left(\frac{\partial u''_i}{\partial x_j} + \frac{\partial u''_j}{\partial x_i} \right)} - \overline{\omega'_i \omega'_i \frac{\partial u''_j}{\partial x_j}} + \frac{2}{\text{Re}} \overline{\epsilon_{ikl} \frac{\partial \omega'_l}{\partial x_k} \frac{1}{\rho} \frac{\partial}{\partial x_j} \left[\mu \left(\frac{\partial u''_i}{\partial x_j} + \frac{\partial u''_j}{\partial x_i} - \frac{2}{3} \frac{\partial u''_m}{\partial x_m} \right) \right]} + \\ & 2 \overline{\omega'_l \epsilon_{lki} \frac{1}{\rho^2} \frac{\partial \rho}{\partial x_k} \frac{\partial p}{\partial x_i}} \end{aligned} \quad (31)$$

Only two terms are non-negligible in the enstrophy transport equation, the first term on the right hand side of equation which represents the interaction between the strain-rate tensor and vorticity and the third term which represents the interaction between vorticity and the shear-stress tensor. Figure 8a shows the time evolution of these terms. The first term is found to be positive and hence causes the enstrophy to increase initially. Thus the initial rise in the vorticity shown in figure 9 can be attributed to the production of enstrophy by the strain rate tensor. The rise for model 2 is significantly larger than for model 1, indicating a stronger solenoidal field.

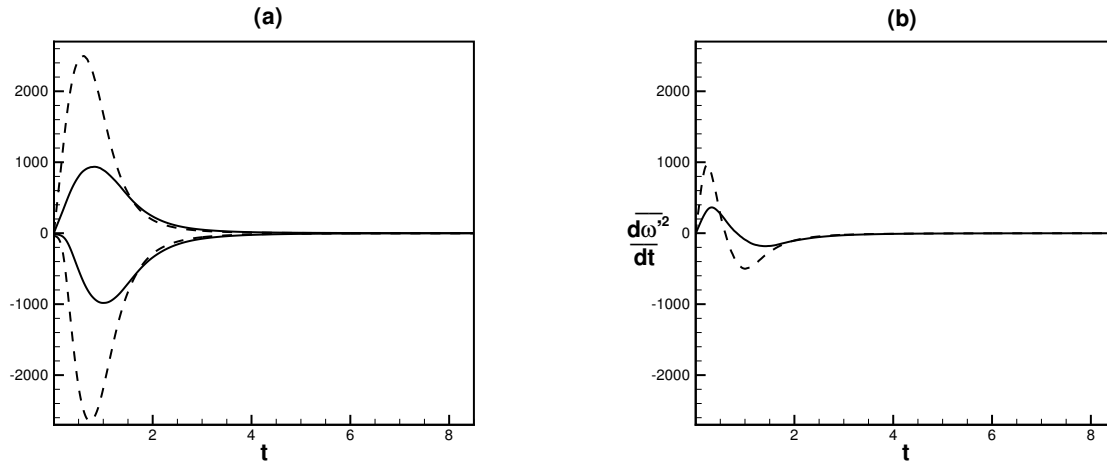


Figure 8. Shows the results of the enstrophy budget for models 1 and 2 at 8000K. (a) Shows the enstrophy production and dissipation terms. The positive terms indicate vortex stretching and the negative terms indicate viscous effects. (b) Shows the right hand side of the enstrophy transport equation. — represents model 1 and - - - represents model 2.

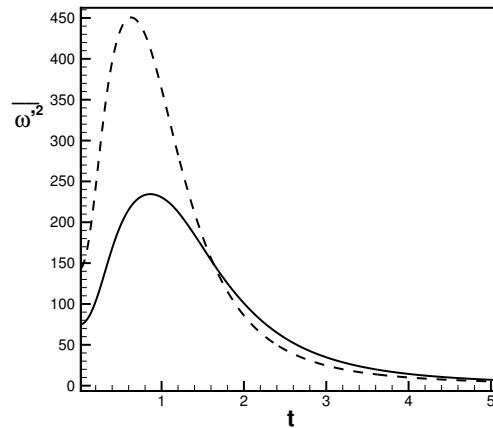


Figure 9. Figure shows the time evolution of vorticity for the two models 1 and 2 at 8000K. — represents model 1 and - - - represents model 2.

The other term can be interpreted as the interaction between the enstrophy and viscous dissipation. It is a negative term and hence is responsible for the dissipation of energy stored in the vortices. Again, it is to be noted that the enstrophy decay is stronger for model 2 than for model 1. Initially the strain rate tensor's contribution is strong and thus serves to increase the vorticity. Over time, the dissipation becomes significantly stronger and causes the vorticity to decrease. Figure 8b shows a plot of the total right hand side of the enstrophy transport equation in time and so represents the cumulative effect of the different terms plotted in figure 8a.

Figure 10 shows the energy spectra for both the models at $t = 5.1$. Model 2 is found to have more energy in the larger length scales in comparison to model 1. In the intermediate and small length scales, model 1 has more energy than model 2.

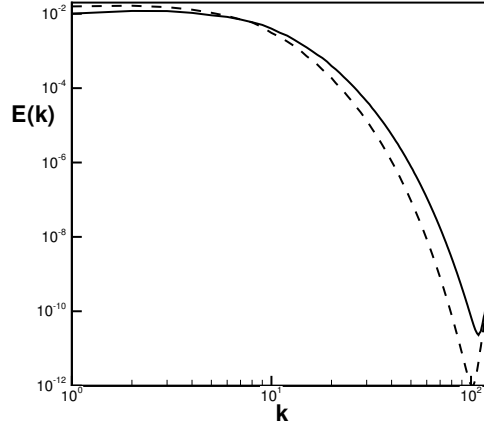


Figure 10. Energy spectra at $t = 5.1$. — represents model 1 and - - - represents model 2.

V. Summary

High temperature effects on decaying isotropic turbulence is studied using DNS. A compressible Navier-Stokes flow solver is developed for the purpose. The solver uses Fourier-spectral spatial discretization, a skew-symmetric form of the non-linear terms to suppress aliasing error, a fourth order explicit Runge-Kutta time integration method for temporal advancement and is parallelized using message passing interface (MPI). The flow solver is validated using benchmark problems.

An L.T.E. based high temperature physical model for air is suggested which accounts for vibrational excitation and chemical reactions. DNS results for decaying isotropic turbulence obtained using this high temperature model (model 2) are compared to those obtained using a calorically perfect gas model for air (model 1). Simulations at 300 K show both models predicting same results. This is to be expected as at these temperatures there are no high temperature effects and so model 2 should physically reduce to model 1.

DNS of decaying isotropic turbulence is then conducted at an initial background temperature of 8000 K using both models 1 and 2. q^2 and Re_λ plots in time indicate a faster decrease for model 2. This is found to be due to an increased dissipation observed for model 2. The total dissipation is decomposed into a solenoidal component and a dilatational component. For both models, the solenoidal component is found to dominate. Between models 1 and 2, the solenoidal component is found to be larger for model 2, resulting in a larger total dissipation. Mean temperature evolution in time is also compared for the two models. Model 2 shows lower mean temperature as part of its internal energy is stored in the vibrational energy mode and also used for chemical reactions. Budgets are computed for different terms on the right hand side of the turbulent kinetic energy (TKE) equation and the enstrophy transport equation. TKE budgets show that even at high temperatures the dissipation term dominates. Dissipation is found to be higher for model 2. Only other non-zero term is the pressure dilatation term which initially is higher for model 2 but becomes negligible in time. The enstrophy budget indicates that vortex stretching dominates initially causing enstrophy production but later solenoidal dissipation becomes strong, causing enstrophy to decrease. These processes are stronger for model 2. Energy spectra plotted at $t = 5.1$ shows more energy in smaller length scales for model 1 and more energy in larger length scales for model 2.

VI. Acknowledgements

The Computational resources required for this work are provided by the P. G. Senapathy Center for Computing Resources and the Department of Aerospace Engineering at the Indian Institute of Technology, Madras, India.

References

- ¹Kovaszny, L. S., “Turbulence in supersonic flow,” *Journal of aeronautical sciences*, Vol. 20, No. 10, October 1953, pp. 657–674.
- ²Chu, B.-T. and Kovaszny, L. S., “Non-linear interactions in a viscous heat-conducting compressible gas,” *Journal of fluid mechanics*, Vol. 3, No. 5, February 1958, pp. 494–514.
- ³Samtaney, R., Pullin, D., and Kosovic, B., “Direct Numerical simulation of decaying compressible turbulence and shocklet statistics,” *Physics of Fluids*, Vol. 13, No. 5, May 2001, pp. 1415–1430.
- ⁴Ristorcelli, J. R. and Blaisdell, G. A., “Consistent initial conditions for the DNS of compressible turbulence,” *Physics of Fluids*, Vol. 9, No. 1, January 1997, pp. 4–6.
- ⁵Zeman, O., “On the decay of compressible isotropic turbulence,” *Physics of Fluids A: Fluid Dynamics*, Vol. 3, No. 951, 1991.
- ⁶Erlebacher, G., Hussaini, M. Y., Kreiss, H. O., and Sarkar, S., “The analysis and simulation of compressible turbulence,” *Theoretical and Computational Fluid Dynamics*, Vol. 2, July 1990, pp. 73–95.
- ⁷Blaisdell, G. A., *Numerical simulation of compressible homogeneous turbulence*, Ph.D. thesis, Stanford University, January 1991.
- ⁸Sutherland, W., “The viscosity of gases and molecular force,” *Philosophical Magazine Series 5*, , No. 36, 1893, pp. 507–531.
- ⁹Boulos, M. I., Fauchais, P., and Pfender, E., *Thermal plasmas: fundamentals and applications*, Springer Science+Business Media, New York, 1994.
- ¹⁰Ghosh, S., *Direct numerical simulation of the interaction of a laser-induced plasma with isotropic turbulence*, Ph.D. thesis, University of Minnesota, September 2008.
- ¹¹Rogallo, R. S., “Numerical experiments in homogeneous turbulence,” Technical Memorandum 81315, National aeronautics and space administration, September 1981.